International Journal of Hydrogen Energy 58 (2024) 525–535

Contents lists available at ScienceDirect

International Journal of Hydrogen Energy

journal homepage: www.elsevier.com/locate/he

Experimental and theoretical assessment of the enhanced hydrogen adsorption on polycyclic aromatic hydrocarbons upon decoration with alkali metals

Anna Maria Reider [a,*], Siegfried Kollotzek [a], Paul Scheier [a], Florent Calvo [b,*], Ersin Yurtsever [c], Fernando Pirani [d], Massimiliano Bartolomei [e], Marta I. Hernández [e], Tomás González-Lezana [e], José Campos-Martínez [e,*]

[a] Institut für Ionen Physik und Angewandte Physik, Universität Innsbruck, Technikerstr. 25, Innsbruck, A-6020, Austria
[b] Université Grenoble Alpes, CNRS, LiPhy, Grenoble 38000, France
[c] Department of Chemistry, Koç University, Rumelifeneri Yolu, Sariyer, 34450 Istanbul, Turkey
[d] Dipartimento di Chimica, Biologia e Biotecnologie, Università di Perugia, Perugia, Italy
[e] Instituto de Física Fundamental C.S.I.C., Serrano 123, Madrid, E-28006, Spain

ARTICLE INFO

Keywords:
Polycyclic aromatic hydrocarbons
Helium nanodroplet experiments
Alkali decoration
Enhanced hydrogen storage

ABSTRACT

Hydrogen storage by physisorption on carbon-based materials is limited by comparatively low adsorption energies. However, decoration of the carbon substrate with alkali, alkaline earth, or other metal atoms has been proposed as a means to enhance adsorption energies. The decoration affects also the stability of these materials since it makes them more stable and resilient in the repeated cycles of charge and discharge that would be required for a good material devoted to storage. We investigate hydrogen storage capacities of small polycyclic aromatic hydrocarbons (PAHs) cations grown in ultracold helium nanodroplets by analyzing the ion abundances and stabilities. The observations are assessed with quantum chemical calculations and atomistic simulations. It is experimentally shown that the addition of an alkali ion significantly enhances the hydrogen adsorption of the studied PAHs, up to 25% over the bare PAH in the experimental conditions studied here, and the simulations confirm this general trend except for some minor residual discrepancies in the special stabilities (magic numbers). Several approaches to study larger and different PAH compounds are also proposed, and for all cases it is found that alkali decoration increases energy stability by more than 100%.

1. Introduction

The increasing global demand for clean and sustainable energy sources has intensified the search for efficient and environmentally friendly technologies. The use of hydrogen as an energy vector is nowadays widely recognized as one of the main resources to reach the mentioned goals [1–3]. However, to serve as the desirable clean, efficient and renewable source (or reservoir) of energy, many challenges need to be surmounted. One of them is the proper way of production [4]. Regardless of the method used to produce hydrogen (blue, green or any other label intended to denote the origin of production), there are still many open questions. Furthermore, a convenient form of transportation and storage is needed to deliver the energy to the final consumer. It is this last point where we will center our attention [5,6], particularly on the adsorption storage issue, for which there exist several alternatives [7–12]. In addition to the compressed gas or cryogenic liquid, storage in solid form is one of the more suitable ways for the hydrogen fuel. This includes using the absorption on metal hydrides and complex hydrides [13,14], as well as various nanoporous materials [15,16] and in particular metal–organic frameworks (MOF) [17] or zeolites [18,19].

In recent years, attention has increasingly been devoted to the potential of polycyclic aromatic hydrocarbons (PAHs) as novel hydrogen storage materials or as prototypes of carbon nanoporous materials [20–23]. PAHs, characterized by their large conjugated π-systems, offer high theoretical hydrogen storage capacities and desirable physicochemical properties that make them attractive candidates for addressing the limitations of existing storage technologies. Nevertheless, the practical utilization of PAHs for hydrogen storage is hindered by their intrinsic thermodynamical and kinetic constraints such as weak adsorption energies and slow adsorption and desorption rate constants.

* Corresponding authors.
E-mail addresses: anna-maria.reider@uibk.ac.at (A.M. Reider), florent.calvo@univ-grenoble-alpes.fr (F. Calvo), jcm@iff.csic.es (J. Campos-Martínez).

https://doi.org/10.1016/j.ijhydene.2024.01.244
Received 19 October 2023; Received in revised form 15 January 2024; Accepted 20 January 2024
Available online 25 January 2024
0360-3199/© 2024 The Author(s). Published by Elsevier Ltd on behalf of Hydrogen Energy Publications LLC. This is an open access article under the CC BY-NC-ND license (http://creativecommons.org/licenses/by-nc-nd/4.0/).

The ultimate target storage for light duty vehicles drawn by the Office of Energy Efficiency & Renewable Energy [24] reaches values of 0.065 gravimetric capacity (kgH_2/kg system) and 0.050 volumetric capacity (kgH_2/L system). The adsorption of hydrogen inside nanoporous materials is attractive since it is of a physical nature in which only weak forces are involved and there is no formation or breaking of chemical bonds, with typical physisorption energies around 50–60 meV [25]. This weak interaction has the drawback that the mentioned gravimetric or volumetric capacities are low, and therefore it has been suggested to add some dopants that could increase such a storage capacity. For example, using alkali or alkaline earth metals, it was early found that storage capacities could be increased by 5% *wt* [26–28] in some fullerenes, as well as in carbon nanotubes (CNTs) [29,30]. Together with PAHs, these compounds constitute typical carbon prototypes for the study of hydrogen adsorption on carbon-based materials. The benefit of alkali decoration has also been found in popular MOF materials [31].

Alkali metals, known for their ability to enhance hydrogen storage properties, can profoundly influence the adsorption and desorption behavior of PAHs by modulating the electronic structure and charge transfer interactions. Decorating PAHs with alkali metals provides a unique avenue to enhance hydrogen storage capacities, and to improve thermodynamic stability, thus preventing the substrate from destruction in the reversible adsorption process [28,32]. It is expected to also potentially accelerate hydrogen release kinetics, thereby enabling more efficient and practical hydrogen storage systems. Moreover, it must be recognized that both adsorption and desorption processes are very much related to one another and, thus, a large energy release in the adsorption process means equivalent energy needed to recover the adsorbate, i.e, the hydrogen. There have been several suggestions on how to address this specific issue and one of the most common is to use electric charges or voltages [33,34]. Therefore, employing a charged material is a natural way to approach this possibility.

In a previous investigation [35], enhanced hydrogen adsorption on alkali (cesium) decorated C_{60} grown in ultracold He nanodroplets was observed as well as the appearance of some anomalies in the size distribution manifested in the ion abundance of the mass spectrum. In this work we have carried out similar experimental measurements with a new experimental setup [36,37] that allows higher ion yields which, together with an excellent resolution in the mass spectra, lead to an accurate determination of the relative populations of cluster sizes. After comparison of the same quantity recorded for hydrogen clusters in contact with bare PAHs, this allows for a direct estimation of the effects of sodium decoration on the propensity for hydrogen attachment. Experimental results are then compared to quantum simulations based on force fields carefully parametrized on high-level electronic structure calculations.

In particular, hydrogen adsorption is investigated on bare and sodium-decorated cationic complexes, respectively denoted as $[PAH]^+$ and $[PAH\text{-}Na]^+$. Here, we explore how the hydrogen molecules attach to the compound and, more interestingly, how much increase in hydrogen storage can be reached by adding a sodium atom to the complex. In this sense, the experimental data can shed light onto the generic effects of alkali decoration, and the more specific size effects leading to further enhancement in the adsorption propensity of the polyaromatic cation. The choice of sodium as the alkali to decorate the PAH is very appealing [28,38], since despite being larger than lithium, one of the most popular alkalis for energy applications, it is also much more sustainable.

The present work focuses on naphthalene ($C_{10}H_8$) as the specific PAH on which measurements and atomistic modeling were conducted, and hydrogen clusters were thus investigated around the following complexes,

- naphthalene cation, $[Naph]^+$;
- protonated naphthalene, $[H\text{-}Naph]^+$;
- sodium-naphthalene cation, $[Naph\text{-}Na]^+$;
- sodium-protonated naphthalene, $[H\text{-}Naph\text{-}Na]^+$;

where for brevity naphthalene is simply denoted as Naph. In addition, our models allow tentative predictions on related, but essentially larger complexes, thereby exploring the effects of PAH size:

- benzene (C_6H_6) and sodium-benzene cations, $[benzene]^+$ and $[benzene\text{-}Na]^+$;
- anthracene ($C_{14}H_{10}$) and sodium-anthracene cations, $[anthracene]^+$ and $[anthracene\text{-}Na]^+$;
- corannulene ($C_{20}H_{10}$) and sodium-corannulene cations, $[corannulene]^+$ and $[corannulene\text{-}Na]^+$;
- coronene ($C_{24}H_{12}$)and sodium-coronene cations, $[coronene]^+$ and $[coronene\text{-}Na]^+$.

This paper aims to comprehensively explore the relevance and potential of Naph and related PAHs decorated with sodium for hydrogen adsorption. To this aim, the fundamental principles underlying the interaction between alkali metals and PAHs, including the electronic and structural modifications induced by decoration, will be scrutinized. Moreover, the impact of alkali metal decoration on key hydrogen storage parameters such as storage capacity and stability will be addressed. The challenges associated with the synthesis, characterization, and integration of PAHs decorated with alkali metals into practical hydrogen storage devices will also be discussed.

The paper is divided into a section devoted to experimental and theoretical methods, followed by the presentation of results and a final concluding section.

2. Methods

In this work, the opportunities opened by carbon-based nanomaterials for their use in hydrogen storage are studied from a very fundamental perspective in the gas phase. The use of superfluid helium nanodroplets as the initial embedding medium enables an accurate and rigorous selection of clusters, as a function of the number of hydrogen molecules, thereby providing some direct insight into the relative stability of the complexes decorated with hydrogen and, through appropriate comparison between bare- and sodium-decorated cations, into the effects of sodium doping. Below, we describe the main features of the apparatus and the way measurements were conducted, before giving some details on our computational modeling of the same complexes.

2.1. Experimental

Experiments carried out in this work have been explained in detail elsewhere [37]. The setup, shown in Fig. 1, is briefly described as follows. Helium nanodroplets (HNDs) are produced via supersonic expansion of ultra-pure helium gas (Messer, purity 99.9999%) with a stagnation pressure of 20 bar through a 5 μm pinhole nozzle into ultrahigh vacuum. The nozzle is cooled with a closed-cycle cryo cooler (Sumitomo Heavy industries RDK-408D2) and counter-heated with an ohmic resistor operated with a PID controller (Lakeshore Model 331) to 8.8 K. According to Gomez et al. [39], these conditions result in an average droplet size of about two million He atoms. To prevent the destruction of HNDs by collisions with shock fronts, the resulting helium jet is then passed through a 0.5 mm skimmer (Beam Dynamics, Inc.) located 10 mm after the nozzle. HNDs are ionized by a Nier-type electron impact ionization unit directly after the skimmer. The ion source is operated at an electron energy of 70 eV and an electron current of 200 μA.

The next steps involve forming He_n^+ charge centers from the initially charged species, He^+, and the subsequent formation of He_2^+ and larger clusters consisting of a tightly bound He_3^+ core surrounded by polarized, neutral helium atoms [40–43]. Once the droplets are charged, they

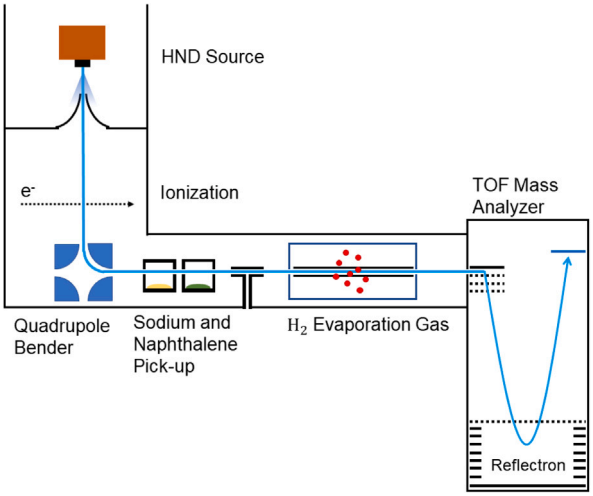


Fig. 1. Experimental setup used to attach H_2 molecules to cationic naphthalene-sodium clusters embedded in helium nanodroplets. The ionized and size-to-charge-selected HNDs are first doped with H_2 that is diffusing back from the evaporation cell. Subsequently, sodium and naphthalene are picked up and clusters can form. Helium is then stripped from the embedded cluster ions by collisions with H_2 gas at room temperature in the evaporation cell, leading to the ejection of low-mass ions from the shrinking droplets. These ions are analyzed in a time-of-flight mass spectrometer.

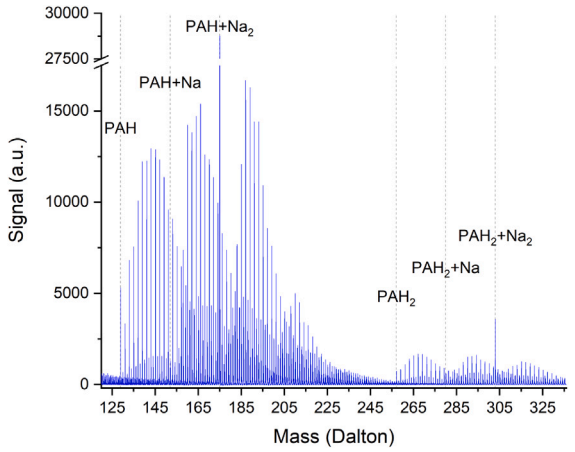


Fig. 2. Typical mass spectrum of cationic bare- and sodium-decorated naphthalene complexes, further solvated by H_2 molecules. The pressure of 1.24×10^{-4} mbar leads to the solvation of mixed naphthalene-sodium ions with, on average, 10 hydrogen molecules. The labeling of $PAH_m + Na_k$ guides the eye for each solvation series of $[Naph_m\text{-}Na_k]^+$ and $[H\text{-}Naph_m\text{-}Na_k]^+$.

are mass-per-charge filtered in the quadrupole bender, resulting in droplets consisting of approximately 3×10^5 He atoms per charge. This yields a mean charge state of the HNDs of about 7 when they subsequently enter the pick-up region, filled with pure naphthalene or sodium-naphthalene vapor. Even though the substances are heated in separated, ohmically heated ovens, their similar evaporation pressures, as well as the geometric construction, lead to a gas mixture. Following cluster formation, the doped HNDs enter an RF-hexapole filled with room-temperature hydrogen gas (pressures in the range (1.24–4.75) $\times 10^{-4}$ mbar, all pressures being corrected for the corresponding ion gauges). This elevated pressure inevitably causes the diffusion of H_2 into the previous chambers, reaching back to the quadrupole bender and the ion source. Consequently, the H_2 molecules are most likely the first species to be picked up into the HNDs (see Supplementary Material, section 1). The ion-induced dipole interaction draws the H_2 towards the He charge centers, where charge transfer then results in the formation of H_2^+. Additional H_2 molecules lead to the formation of $(H_2)_nH_3^+$ ionic cores. Due to the low proton affinity of H_2 (4.38 eV [44]), this ion is the perfect proton donor for almost any dopant inside HNDs [37]. Subsequently, due to their high polarizability compared to helium, sodium and naphthalene are attracted to the charge centers. When the pick-up region is filled with a mixture of sodium-naphthalene gas, two comparably probable processes occur:

- If H_3^+ reacts first with sodium, the main ionic product is Na^+ [43];
- If naphthalene reaches the charge center first, it reacts with H_3^+ to form $[H\text{-}Naph]^+$ due to the high proton affinity of the PAH.

Every further arriving dopant (up to several Naph molecules or Na atoms) will simply attach to an already existing ionic core, leading to the formation of $[H\text{-}Naph_m\text{-}Na_k]^+$ as well as $[Naph_m\text{-}Na_k]^+$. The binding energy will be transferred to the surrounding He, leading to the evaporation of about 1600 He atoms per eV from the surface of the HND. In this way, the surrounding helium matrix can quench the excess energy that might otherwise cause the clusters to fragment. The doped HNDs then move into the RF hexapole evaporation cell, where multiple collisions with H_2 lead to the solvation of the ions with hydrogen by replacing He atoms, and additionally cause the HNDs to shrink via evaporation of He from the droplets. The increasing Coulomb repulsion due to the shrinking of the droplets leads to sequential ejection of charge centers, including protonated and non-protonated sodium-naphthalene cluster ions, often solvated with hydrogen molecules. Typically, 10^5 He atoms have to be removed to eject the next ionic core [36], meaning that several thousands of He atoms must be replaced by H_2 molecules. The ions ejected from the droplets at low hydrogen pressures are solvated with several hundreds of hydrogen atoms. Subsequent collisions of these ejected ions with hydrogen will gradually reduce this number to a desirable value. Thus, a high hydrogen pressure in the evaporation cell results in fewer H_2 molecules solvating the ions. These complexes can then be analyzed in a time-of-flight mass spectrometer (Q-TOF Ultima Waters/Micromass).

Fig. 2 displays a mass spectrum obtained upon pickup of sodium and naphthalene into multiply charged HNDs and subsequent evaporation of the He matrix by multiple collisions with room-temperature hydrogen gas. The mass spectrum is dominated by $[Naph_m\text{-}Na_k]^+$ as well as $[H\text{-}Naph_m\text{-}Na_k]^+$ ions solvated with several H_2 molecules. The dashed lines indicate the position of pristine $[Naph_m\text{-}Na_k]^+$ cluster ions ($m = 1, 2$ and $k = 0, 1, 2$) that are not solvated by molecular hydrogen, where the nomenclature of $PAH_m + Na_k$ emphasizes the presence of both ionized and protonated complexes. Additionally, experiments for different hydrogen pressures in the evaporation cell were carried out to confirm intensity anomalies at specific numbers of hydrogen molecules attached.

2.2. Theory

Different theoretical approaches were considered to model bare and sodium-decorated PAH cations embedded in hydrogen clusters. These models rely on different approximations and levels of coarse-graining, making them appropriate to describe different size ranges and different PAHs as well. Both approaches described below are based on semiempirical models, carefully parametrized on dedicated electronic structure calculations on small systems but mainly differ from one another in the treatment of the H_2 molecules, taken fully atomistically or as a single site for computational efficiency purposes. The most detailed model, which approximates H_2 as a rigid rotor (rr), was developed more specifically for the naphthalene PAH, for which the experiments discussed above were carried out. A simplified model, in which H_2 is coarse-grained as a pseudo atom, was developed with the aim of being transferable to larger numbers of hydrogen molecules, and much larger PAHs as well. In either model, the complete interaction potential is the sum of two main parts, corresponding to the PAHs

interacting with all H_2, plus the interactions between any different pairs of hydrogen molecules, which for a system with n hydrogen molecules can be summarized as

$$V_{\text{tot}} = \sum_{i}^{n} V_i[\text{PAH} - \text{H}_2^{(i)}] + \frac{1}{2}\sum_{i\neq j}^{n} V_{ij}[\text{H}_2^{(i)} - \text{H}_2^{(j)}] \quad (1)$$

The two complementary models are described in the following subsections, namely their functional forms and the set of *ab initio* data used to parametrize them. The computational methods based on these potential energy surfaces used to characterize the structure and energetic properties of hydrogen-coated, bare and sodium-decorated cationic PAHs are discussed next.

2.2.1. Hydrogen as a rigid rotor

The first model was constructed following earlier efforts on the similar coronene PAH interacting with the cations K^+, Cs^+ [45], and also for cesium ions embedded in hydrogen clusters [46]. The model assumes the PAH substrate, possibly decorated with one sodium atom, to be rigid, as well as all surrounding H_2 molecules being treated as rigid rotors. The atomic coordinates of the bare and decorated naphthalene substrates were optimized at the MP2 level of theory, using the aug-cc-pVDZ [47] basis set. Details about these optimized structures are given as Supplementary Material.

The interaction potential $V_{\text{tot}}^{\text{rr}}$ between the hydrogen molecules in the rigid rotor model and the cationic substrate, $V_i[\text{PAH} - \text{H}_2^{(i)}]$ in Eq. (1), is represented analytically using a sum of electrostatic (V_{elec}) and non-covalent ($V_{\text{NC}}^{\text{rr}}$) contributions,

$$V_{\text{tot}}^{\text{rr}} = V_{\text{NC}}^{\text{rr}} + V_{\text{elec}}. \quad (2)$$

The electrostatic contribution is a simple sum of Coulomb terms, with point charges placed along the axes of the H_2 molecules and on various sites of the complex, as described in the Supplementary Material. The so-called improved Lennard-Jones (ILJ) functional form [48] was employed to describe the non-covalent contribution. Its analytical form includes a short-range due to size-repulsion and a long-range term arising from dispersion and induction attraction, as also detailed in the Supplementary Material.

The various parameters entering the rr model were adjusted to reproduce a set of accurate electronic structure reference data, obtained here at the coupled cluster level of theory with single, double, and perturbative triple excitations [CCSD(T)], evaluating the interaction energies by extrapolation to the complete basis set (CBS) limit by applying the two point correlation energy method of Halkier et al. [49,50]. This approach consists in properly combining counterpoise corrected CCSD(T) energies [51] obtained with the aug-cc-pVDZ basis set with those at the Hartree–Fock and MP2 levels obtained with the aug-cc-pVDZ and aug-cc-pVTZ basis sets. In post-HF calculations, only the Na and C first inner orbitals are considered as frozen, while all outer orbitals, as well as the inner shell of H_2, are fully correlated.

Different configurations were considered for the interaction between the cationic substrate and a single H_2 molecule, as detailed in the Supplementary Material. All the reported interaction energies are defined relative to those of the infinitely separated moieties. Electronic structure calculations were carried out using the Molpro2012.1 software package [52].

Regarding the interaction between pairs of rigid hydrogen molecules $[\text{H}_2^{(i)} - \text{H}_2^{(j)}]$, the second term in Eq. (1), it can also be expressed as a sum of non-covalent plus electrostatic contributions, according to the procedure described in Ref. [46]. This interaction depends on the Jacobi coordinates, namely the modulus of the vector $\vec{r}_{ij}$ between the centers of mass of the two diatomic molecules and the angles θ_a and θ_b between the previous vector and the H_2 internuclear distances, as well as the torsion angle ϕ_{ab}, and it reproduces very well the reference results from Patkowski et al. [53].

2.2.2. Hydrogen as a united atom

In order to model larger cationic substrates or a significant number of hydrogen molecules exceeding a few dozens, it is desirable to employ a simpler potential that retains the important features of the interaction at the atomistic level, neglecting the rotational motion of H_2 by treating it as an effective pseudoatom. This approach was successfully applied in the past [54] for the strongly related problem of neutral PAH molecules [55] and PAH clusters [56] embedded in hydrogen clusters, and naturally it is tempting to extend it to the case of sodium-decorated PAH cations and assess its performance in comparison to the previously described model and the new experiments.

The interaction potential $V_{\text{tot}}^{\text{cg}}$ for the coarse-grained representation, the term $V_i[\text{PAH}-\text{H}_2^{(i)}]$ in Eq. (1), is once more the sum of a non-covalent component over all atomic sites of the substrate (carbon and hydrogen atoms of the PAH, plus the alkali), and a polarization contribution that accounts for the lowest-order electrostatic energy between the (chargeless) H_2 pseudoatom and the distribution of partial charges among the substrate, producing an electric field on each hydrogen site:

$$V_{\text{tot}}^{\text{cg}} = V_{\text{NC}}^{\text{cg}} + V_{\text{polar}} \quad (3)$$

in which we have emphasized that the expressions for the noncovalent component differ between the rr and cg representations through the superscripts in V_{NC}. The complete expressions for the various terms of the above potential are explicited in the Supplementary Material.

The functional form chosen for the interaction between hydrogen and the alkali decorated cationic complex is the same as in our previous work in which the substrates were bare, cationic PAHs [54,55]. The same parameters are thus used for the interactions between pseudo hydrogen atoms and the carbon and hydrogen atoms of the substrate. It is therefore also natural to follow the very same strategy to determine the reference electronic structure data and parameters for the sodium-decorated complexes. Regarding the cationic complexes, equilibrium geometries were optimized with density-functional theory employing the M06-2X functional and the 6-31G(d,p) basis set, and they are provided in the Supplementary Material. The interaction energies between the complexes and the H_2 molecules were calculated using single-component-scaled MP2 (SCS-MP2) with the aug-cc-pVTZ basis set. The SCS-MP2 approach was shown to give results in very good agreement with CCSD(T) calculations [54]. In the presence of the alkali decoration, the description of the complex with interaction sites exactly at the atomic positions was found to reproduce rather poorly the *ab initio* interaction energies, especially for H_2 molecules approaching the alkali atom directly. A much greater accuracy was met by adding some interaction sites along the bond between the sodium atom and the nearest carbon neighbors, and considering them as pseudo atomic sites with their specific Born–Mayer repulsive parameters and C_6 and C_8 dispersion terms, but no net charge. From a chemical point of view, these extra sites can be seen as a way to model the ionic–covalent bonds formed by attaching an electron donor atom (sodium) to the much more electronegative carbon framework. The specific positions of the extra sites were adjusted manually and are provided in the Supplementary Material as parts of the detailed geometries of the cationic complexes. In most PAHs, sodium binds to an hexagonal carbon ring, producing 6 such sites, corannulene being an exception with the alkali atom binding on either side of the pentagonal ring and yielding two unequivalent isomers.

Using the available parameters for the cg interaction model between H_2 and the bare cationic PAH [54,55], only the missing parameters describing the interaction of H_2 with the alkali and the extra sites along the alkali–carbon bonds were specifically adjusted to reproduce SCS-MP2 interaction energies. This parameterization step was achieved using the $[\text{benzene-Na}]^+$ cation complex, but additional electronic structure calculations on $[\text{Naph-Na}]^+$-H_2 were also performed and the potential was found to be satisfactorily transferable to such larger PAHs (see Supplementary Material), paving the way to study even larger complexes embedded in hydrogen clusters.

Finally, the interaction term between coarse-grained H_2 molecules, denoted as V_{ij} in Eq. (1), is taken as the Silvera–Goldman potential [56] with the "isolated" set of parameters.

2.2.3. Structural and energetic properties

For both interaction models, the stable structures of bare and sodium-decorated cationic PAH complexes in contact with a variable number of hydrogen molecules were investigated using simulated annealing Monte Carlo optimizations [57]. Here, the system is modeled with a rigid rotor and optimization methods based on the basin-hopping approach [58] when hydrogen is treated as a united atom.

Under the low temperature of the experiments, hydrogen is vibrationally delocalized and methods are needed to incorporate nuclear quantum effects and correct for zero-point energies. In the rr model, the vibrational ground state wavefunction was evaluated using quantum diffusion Monte Carlo (DMC) [59,60]. With this method, the ground state is computed by propagation of a diffusion equation obtained from the time-dependent Schrödinger equation expressed in imaginary time. The ground state is approached by a set of replicas (or walkers) describing different configurations of the particles in the system that are randomly moved at each time step. Here, a specific implementation of the DMC method for rigid bodies was used [61–63], in which the very fast intramolecular modes are taken out. Details of the procedure and parameters used in the calculations are provided as Supplementary Material.

In the united-atom cg model, nuclear quantum effects were accounted for using path-integral molecular dynamics (PIMD), in which the classical positions of the particles are replaced by a ring polymer whose physical extension mimics the natural de Broglie wavelength. In practice, the true quantum mechanical behavior is recovered when the size P of the ring polymers (Trotter number in the path integral framework [64]) increases sufficiently. The method has been described in earlier publications [54,55] and for a N-particle system it practically amounts to performing classical molecular dynamics simulations on extended $N \times P$-dimensional energy surfaces, at a nonzero temperature typically maintained by massive Nosé–Hoover thermostats at $T = 2$ K. More details about the simulations and specific parameters are provided as Supplementary Material. As in the rr model, the initial configurations are always taken as the putative classical global minimum.

3. Data analysis and results

The ion abundances measured with the experimental setup described in the previous paragraphs were extracted from mass spectra such as the one shown in Fig. 2, after a fit by means of a homemade code [65]. They are represented for increasing number of the attached H_2 molecules in the Supplementary Material (see Figs. S1 and S2). It should be emphasized that our experimental apparatus can detect and measure many different species, but we will restrict ourselves to the first set of clusters that can be observed in Fig. 2. These include the following carbon substrates where n is the number of H_2 molecules attached, all involving Naph as the underlying PAH coated with various numbers of hydrogen molecules, namely $[Naph]^+(H_2)_n$, $[H\text{-}Naph]^+(H_2)_n$, $[Naph\text{-}Na]^+(H_2)_n$ and $[H\text{-}Naph\text{-}Na]^+(H_2)_n$.

From this list, the most abundant species observed are the clusters with an extra hydrogen atom on the substrate (protonated Naph), especially when further decorated with sodium. Signals associated with clusters coating the bare Naph cation appear to be almost negligible. However, for the sake of completeness, these clusters were still considered in our modeling.

In the raw ion abundances (Fig. 2), as well as in subsequent fits (see Figs. S1, S2), and for all pressures recorded, features similar to other ionic cluster cases are found, where some peaks are noticeable and clearly distinguished. These local maxima intensities correspond to molecular clusters that are more stable than their respective neighbors and are usually referred to as magic numbers. The evaluations performed at different pressures ensure that there are no anomalies due to size distribution effects.

To facilitate the theoretical interpretation of the ion abundances I_n, the raw intensities shown in Fig. S1 are further processed within the evaporative ensemble framework [66,67]. In this approach, anomalies in the variations of I_n and those of the evaporation energies $\Delta E_n = E_{n-1} - E_n$, E_n being the binding energy of the cluster containing n hydrogen molecules, are connected to each other through an approach that was first proposed by Leidlmair et al. [68] and later in Refs. [69,70]. More precisely, this model simply states that

$$\frac{I_n}{I_{\mathrm{av}}} \approx \frac{\Delta E_n}{\Delta E_{\mathrm{av}}}, \tag{4}$$

where I_{av} and ΔE_{av} are local averages of I_n and ΔE_n. The relation above can be approximately applied under the fulfillment of two main conditions: (i) the observed cluster ions are the unimolecular fragments of larger precursors; and (ii) their internal vibrational modes are not excited at the relevant temperature, the associated heat capacity being vanishingly small. These two conditions are met in the present experiment. In the following, for both experimental and theoretical data, the averages were taken over neighboring cluster sizes using a Gaussian function with a standard deviation $\sigma = 1$.

In Fig. 3 the experimental ion abundance ratios are shown and compared with the corresponding theoretical averages [both terms in Eq. (4)] for the case of hydrogen clusters coated with protonated Naph and with protonated Naph with sodium, with the evaporation energies obtained from DMC calculations based on the rr model. In the case of protonated Naph [Fig. 3(a)], a peak for $n = 2$ is easy to interpret as it corresponds to a very stable configuration with two hydrogen molecules located on the opposite sides of the same hollow ring of the PAH. The next peak corresponds to $n = 5$ in the experiment and $n = 6$ for theory. The discrepancy in the case of $n = 5$–6 appears even though evaporation energies exhibit a local maximum for $n = 5$, followed by a large drop that produces the final more intense peak around $n = 6$ in the theory, as will be further discussed below.

For hydrogen clusters adsorbed on the sodium-decorated protonated naphthalene cation [Fig. 3(b)], there is a clear agreement between theory and experiment for the enhanced stability displayed at $n = 4$, a second magic number being found at $n = 7$ in the experiment but at $n = 6$ in the calculations. Both features as well as the associated discrepancy are similarly found for hydrogen clusters coating the sodium-naphthalene cation (this can be appreciated in Fig. S6 of the Supplementary Material).

The findings in Fig. 3 can be understood from the structures exhibited by the clusters in both cases. For hydrogen adsorption onto (undecorated) protonated Naph, $n = 2$ appears as a very stable compound. It is the lowest-energy structure of the corresponding $[H\text{-}Naph]^+(H_2)_2$ cluster, in which the hydrogen molecules lie near the hollows on opposite aromatic sites of the carbon frame. The next two molecules become adsorbed on energetically less favorable positions, filling successively the next unoccupied hollow positions on the PAH. With two more additional molecules the next rather stable structure is reached for $n = 6$, where each molecule is adsorbing on each side of the carbon structure but slightly displaced to the sides. This situation changes when the alkali atom is present, as it tends to act as a primary binding site to the oncoming hydrogen molecules. This effect can be clearly appreciated in Fig. 4(a), when compared to the undecorated situation, Fig. 4(b).

Our calculations with the rr and cg models indicate that 6 hydrogen molecules are optimal for capping the alkali atom, forming mostly a pentagonal ring with one extra molecule at the top. When an extra molecule is added ($n = 7$), it is adsorbed on the remaining hydrocarbon frame but in a less favorable position, on the other side of the hydrocarbon, as can be seen in Fig. 4(a). This picture of preferential

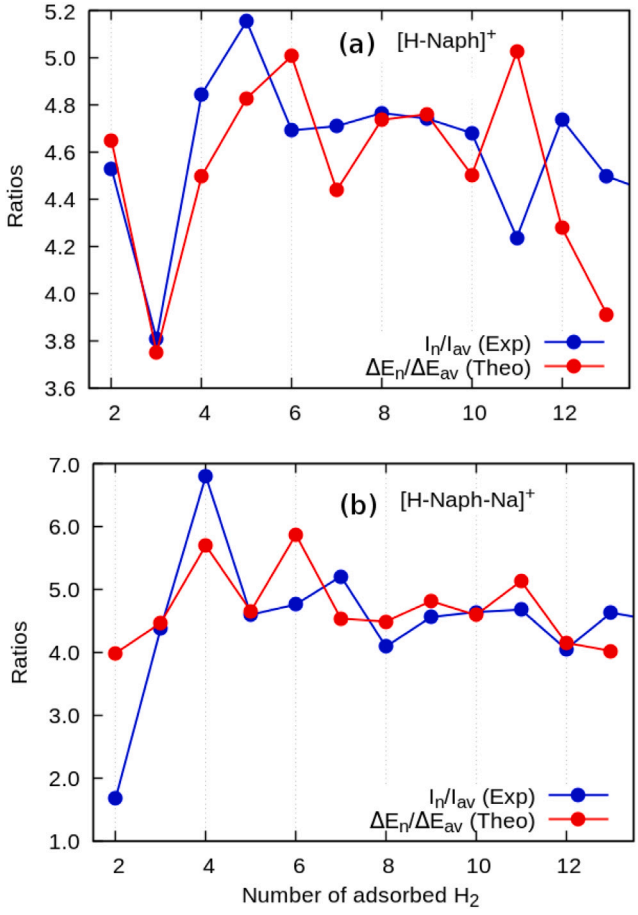


Fig. 3. Ratios of measured ion abundances (blue symbols) and calculated evaporation energies (red symbols), as obtained for (a) $[H\text{-}Naph]^+(H_2)_n$; and (b) $[H\text{-}Naph\text{-}Na]^+(H_2)_n$.

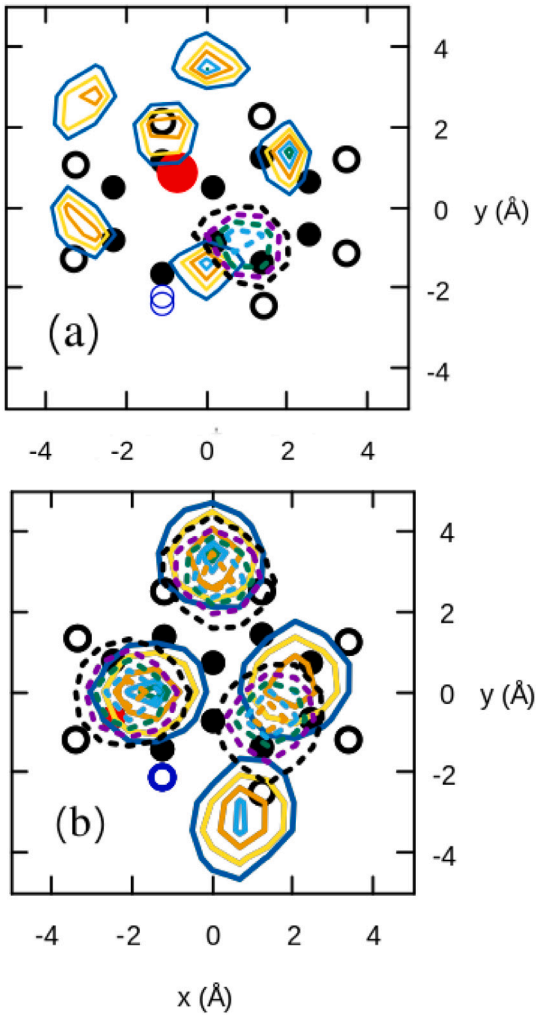


Fig. 4. Probability densities of hydrogen molecules obtained for (a) $[H\text{-}Naph\text{-}Na]^+(H_2)_7$; (b) $[H\text{-}Naph]^+(H_2)_7$, as inferred from DMC calculations with the rigid rotor model. Dashed contour lines highlight probabilities below the naphthalene molecular plane. The full and empty black circles show the positions of the carbon and hydrogen atoms within the naphthalene plane, the blue and red dots indicating the positions of the out-of-plane extra hydrogen atoms bound to the carbon frame at the protonated site, and the sodium atom, respectively.

binding to the alkali before the rest of the complex is expected to be correct from the physical chemistry point of view, owing to the rather different binding energies predicted for H_2 in contact with the bare or the sodium-decorated cations. The difference of one molecule to form a magic number thus suggests that the capping ring could be made of 7 molecules instead of 6, which points at some inaccuracies in our modelings. The coarse-grained model does not capture well the rather anisotropic nature of the interaction between H_2 in the vicinity of the charged sodium atom, and may thus be questionable at small numbers of hydrogen molecules around the cationic complex. The wavefunction determined computationally for the bare (undecorated) case shows broadly localized spots in Fig. 4(b) that account for 2 + 2 hydrogen molecules lying above and below the aromatic plane and 2 + 1 on the lateral sides. In the sodium-decorated complex, 6 of the seven hydrogen molecules arrange in a much tighter way in the immediate vicinity of the sodium cation, the remaining molecule standing on the opposite site of the PAH, with an extent of delocalization that is similar to the undecorated case.

To get further insight into the effects of adding a sodium atom to the hydrocarbon substrate, we have represented in Fig. 5 the variations of the evaporation energies for hydrogen clusters coating the cationic and protonated complexes, further possibly decorated with sodium, for increasing numbers of hydrogen molecules. These data were obtained with the rr model for H_2. The pattern shown in the previous plot, with the 6 particularly localized molecules and one more loosely bound molecule, is consistent with the drop in the evaporation energy predicted just above $n = 6$ in both plots in Fig. 5.

From this figure the effects of sodium decoration on the propensity for hydrogen adsorption on the PAH can be immediately appreciated. In the case of the undecorated (bare) PAH, the evaporation energies are significant with values above 30 meV, but only up to $n = 2$ adsorbed molecules, after which they drop close to 20 meV. These energies remain mostly constant up to $n = 6$–8, then a second drop occurs with values below 15 meV. In the presence of the sodium atom, the evaporation energies are much higher and start above 80 meV, marking drops at $n = 5$ in both cationic and protonated complexes, followed by another drop at $n = 7$ and yet another, weaker drop above $n = 10$.

The mechanism behind the enhancement of the hydrogen adsorption for Na-decorated PAHs stems from the large fraction of the positive charge that is localized on the alkali atom within the PAH complexes. As detailed in the Supplementary Material, a charge distribution analysis of these substrates reveals that most of the positive charge (about 0.7 a.u.) is carried by the Na atom. Accordingly, the H_2-Na interaction takes into account, besides the ubiquitous van der Waals forces, induction and electrostatic contributions. These contributions arise from the interaction between the alkali charge and the H_2 electronic polarizability and permanent electric quadrupole moment, respectively. These fundamental properties are determined by the behavior of electrons confined on the outer orbitals of both interacting partners. Therefore,

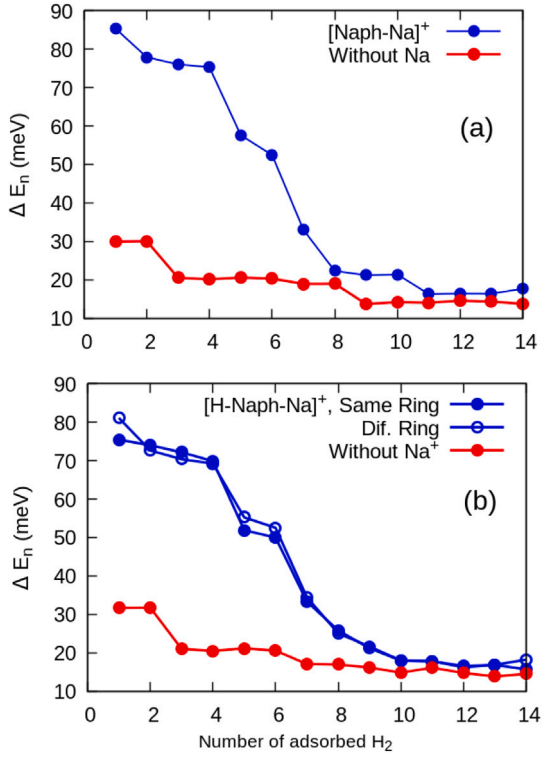


Fig. 5. Evaporation energies of (a) $[Naph]^+(H_2)_n$ and $[Naph\text{-}Na]^+(H_2)_n$ clusters; (b) $[H\text{-}Naph]^+(H_2)_n$ and $[H\text{-}Naph\text{-}Na]^+(H_2)_n$ clusters, as obtained a function of n from DMC calculations using the rigid rotor model. Note that the protonated system has two isomers with the extra hydrogen in the same ring as sodium, or in the other ring, hence the two datasets in panel (b) (see Table S5 in the Supplementary Material).

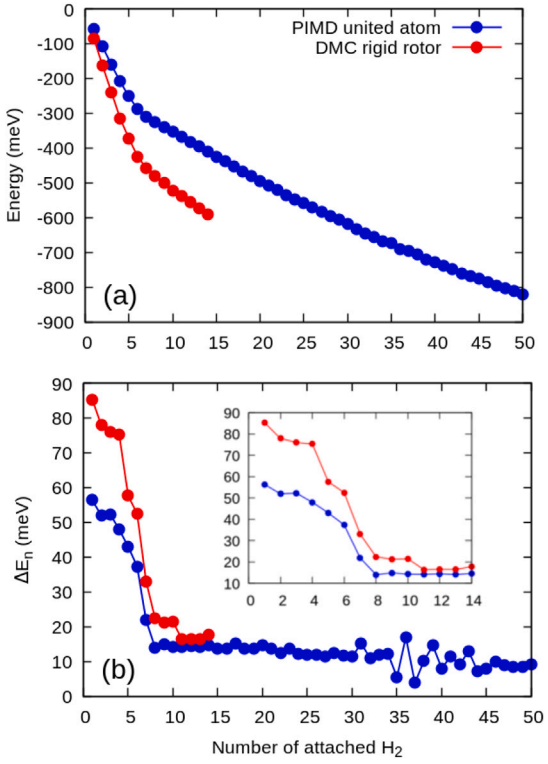


Fig. 6. Comparison of DMC and PIMD results for $[Naph\text{-}Na]^+(H_2)_n$. (a) Binding energies; (b) evaporation energies. In panel (b), the inset highlights the similar results obtained for $n < 15$, inside the dashed box, in the main figure.

such orbitals play the most effective role in the control of strength and anisotropy of the main interaction components. These induction and electrostatic contributions are particularly evident when the diatom is approaching on top of the metal and oriented parallel to the substrate plane, as shown in Fig. S3 of Supplementary Material, where it can be seen that the interaction energy is twice the one for the approach towards the undecorated side. As a consequence, the first (six) H_2 molecules will tend to preferentially place themselves in the proximity of the Na atom, as seen in Fig. 4. In the undecorated substrate, on the contrary, the positive charge is more widely distributed among almost all its atoms (see Tables S3, S4 in the Supplementary Material) so that the resulting induction and electrostatic contributions are negligible with respect to the dominant but weak van der Waals component.

The stabilization effect due to the alkali decoration is thus particularly clear when up to 7 hydrogen molecules are added to the complex, but it holds for the entire range of cluster sizes. Besides Fig. 5, this effect can also be seen in the probability densities of Fig. 4. This stabilization can be also clearly confirmed by looking at binding energies of the Na atom to different PAH (given in Table S15 of Supplementary Material), and the clear improvement in hydrogen binding energies of Naph with Na over the undecorated Naph over the whole range of cluster sizes studied (see Fig. S5 in the Supplementary Material).

The enhanced adsorption effect found upon sodium decoration of protonated Naph is expected to convey to other types of PAH complexes, but to treat them we turn now to the other, simplified model in which hydrogen molecules are treated as pseudo atoms. Fig. 6(a) compares the binding energies $E(n)$ obtained for hydrogen clusters in contact with sodium-decorated cationic Naph, with both the rr model (DMC results at 0 K for $n < 15$) and the coarse-grained model (PIMD results at 2 K for $n \leq 50$), while Fig. 6(b) shows the resulting evaporation energies ΔE_n for the same systems. The generic trends found for the two models are very similar, the main difference residing in the lower magnitude of the binding energies with the coarse-grained model, necessarily leading to lower evaporation energies. This close agreement supports the use of the pseudoatom model for larger systems. In smaller clusters, the discrepancies are inherent to the neglect of preferential orientation of the H_2 molecules towards the alkali cation: the lower energies obtained with the pseudo atom description of hydrogen molecules arise from averaging over orientations, which produces effectively lower bonding strengths. As seen from the reference quantum chemical data shown in the Supplementary Material, the energy of an H_2 molecule approaching the sodium cation from above the PAH plane reduces by about 40% from such an averaging. This weaker binding, within the very same proportion, is directly reflected onto the energetic data shown in Fig. 6, in the small size regime (up to $n = 6$) where the binding energy is dominated by H_2–$Na^{(+)}$ interactions. Such discrepancies have also been reported in earlier studies of other cationic-hydrogen systems [43,46].

Keeping these limitations in mind, Fig. 7 shows the variations of the evaporation energies obtained for hydrogen clusters coating a broader range of bare- and sodium-decorated PAH cationic complexes, namely $[benzene]^+$ and $[benzene\text{-}Na]^+$, $[anthracene]^+$ and $[anthracene\text{-}Na]^+$, $[corannulene]^+$ and $[corannulene\text{-}Na]^+$, $[coronene]^+$ and $[coronene\text{-}Na]^+$, using the pseudo-atom model and PIMD simulations at 2 K. In the corannulene and coronene cases, two isomers were considered in which the sodium cation binds to different carbon rings.

All complexes generally show the same enhanced adsorption effect due to sodium decoration at small sizes, with evaporation energies increasing by a factor of 2 until about 6 molecules are adsorbed, at which stage the evaporation energies for the bare complexes are recovered. Likewise, the stabilization of the PAH due to the addition of the sodium atom is clearly recovered, with a similar behavior as the one noted for Naph. Isomeric effects among the cationic complexes are not significant, except for corannulene, for which the maximum number

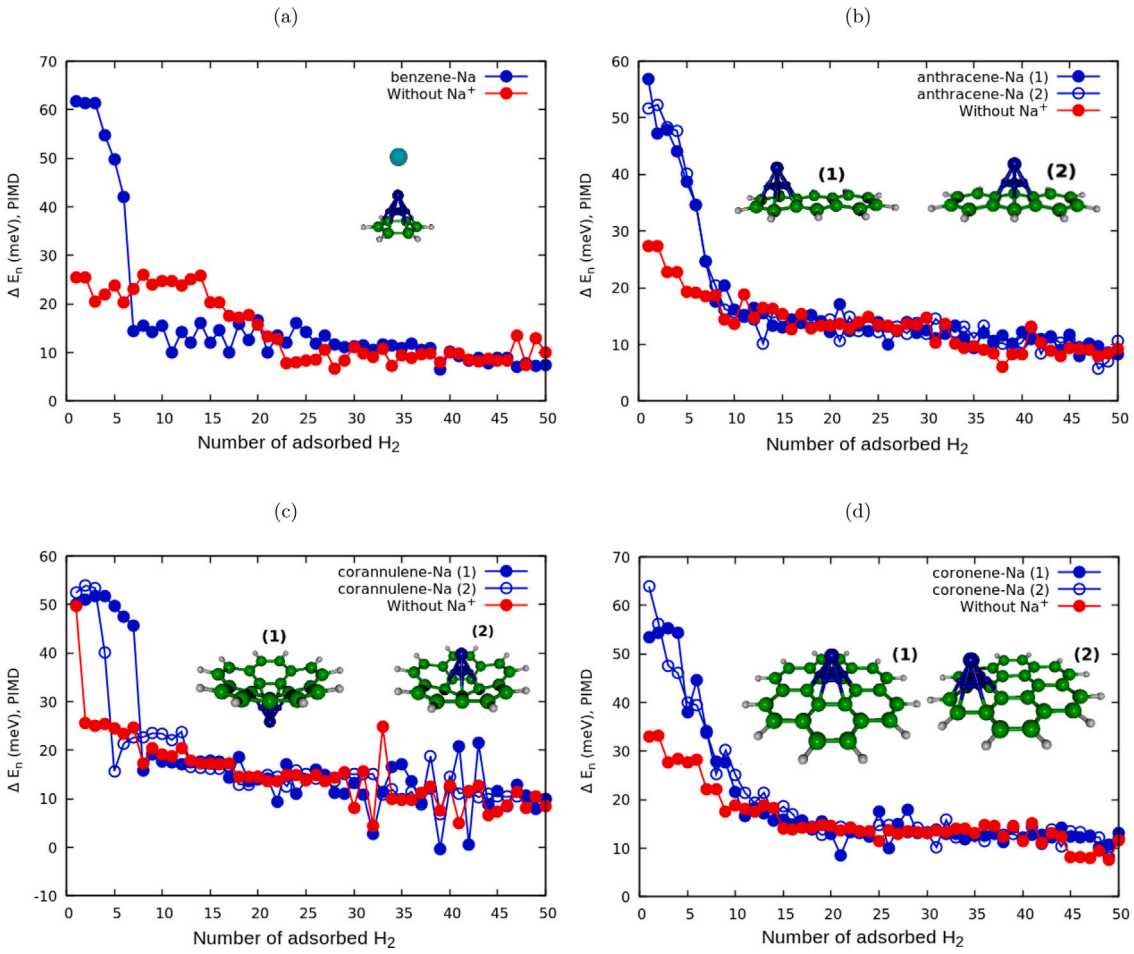


Fig. 7. Evaporation energies $\Delta E_n = E_{n-1} - E_n$ determined for hydrogen clusters coating various cationic PAH complexes possibly decorated with sodium, as obtained from PIMD calculations at 2 K using the coarse-grained model of H_2. (a) Benzene; (b) anthracene; (c) corannulene; (d) coronene. The detailed geometries of the complexes are shown as inset into each corresponding panel — note that for anthracene, corannulene, and coronene 2 unequivalent complexes were considered, differing in the adsorption site of the alkali atom.

of H_2 molecules showing higher evaporation energies caps at $n = 4$ when the sodium atom is adsorbed on the concave side but at $n = 7$ when it is on the convex side. These results are consistent with the very different rooms available for the adsorbed hydrogen in both cases. Interestingly, in the absence of any alkali, the adsorption of a single hydrogen molecule on the corannulene cation is found to be rather strong (about 50 meV instead of about 30 meV on flat PAHs), conveying the very favorable adsorption on the concave side.

More generally, the enhanced adsorption effect can be summarized from the energy difference between hydrogen clusters coating sodium-decorated and bare cationic PAHs, E_n^{ads}, a quantity that is depicted in Fig. 8 as a function of the number of H_2 molecules, for the entire set of complexes investigated here with the coarse-grained model. For all cationic complexes, the adsorption energy exhibits a nearly linear increase at small number of coating hydrogen atoms, reaching a local maximum around 4–6 molecules. For Naph, the same behavior is recovered with the rr model which predicts slightly higher adsorption energies, consistently with the results of Fig. 6

This Fig. 8 confirms the generic behavior common to most cationic PAH complexes, and the peculiarity of the corannulene cation decorated with sodium in its concave side, showing much lower adsorption efficiency. Another remarkable feature for all PAH complexes, except perhaps the later mentioned concave corannulene case, is the local minimum exhibited by the adsorption energy near some particular numbers of adsorbed hydrogens, namely $n \sim 20$ (benzene), 25 (Naph),

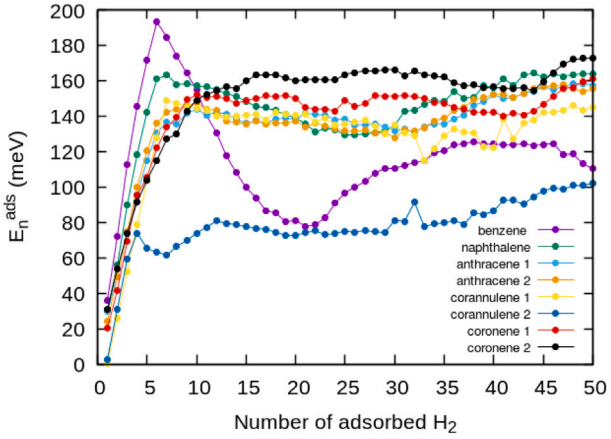


Fig. 8. Adsorption energies defined from the difference between the binding energies of $[PAH\text{-}Na]^+(H_2)_n$ and $[PAH]^+(H_2)_n$, as obtained from PIMD simulations at 2 K using the coarse-grained model for hydrogen, and as a function of n.

30 (anthracene), 35 (convex corannulene), 40 (coronene). These numbers approximately correlate with the amount of hydrogen molecules needed to complete the first solvation shell.

The enhancement in H_2 attachment due to sodium decoration, illustrated from a theoretical point of view in Fig. 8, can also be seen

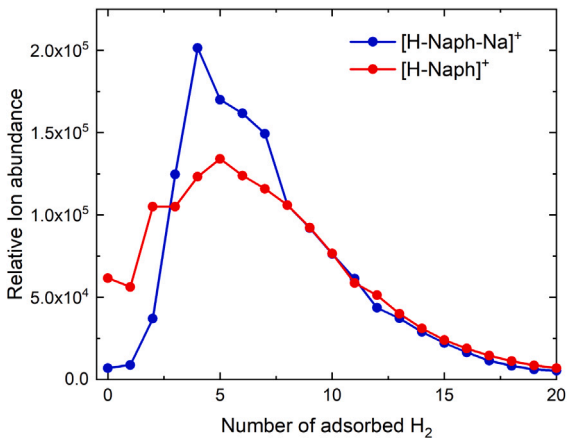


Fig. 9. Relative ion abundances measured for $[H\text{-}Naph]^+(H_2)_n$ and $[H\text{-}Naph\text{-}Na]^+(H_2)_n$ cations, as a function of the number of n. The gain in H_2 absorption for $n = 3$–7 can be clearly appreciated.

from the present experiment carried out on protonated Naph. Fig. 9 shows the ion abundances obtained for hydrogen clusters adsorbed on the bare- and sodium-decorated protonated naphthalene cations.

This figure clearly shows that in the size range $n = 3$–7, capture of H_2 is significantly enhanced due to the presence of the alkali atom, a result that is fully consistent with the theoretical results from Figs. 5 and 7. This gain in hydrogen adsorption efficiency amounts to about 25% but becomes vanishingly small above $n = 8$, a result also in agreement with the computed evaporation energies.

To the best of our knowledge, this figure provides the first experimental evidence of an enhancement of hydrogen attachment upon decorating a PAH substrate with an alkali metal, an improvement in H_2 absorption that has been suggested earlier [26,28,29,31] and experimentally shown here, within the same protocol and experimental setup, and for which we have provided a satisfactory theoretical explanation.

4. Conclusions

The effects of an alkali atom on the propensity for hydrogen adsorption of cationic polycyclic aromatic molecules were experimentally and theoretically investigated. Our approach allows the specific effects of size (number of adsorbed hydrogen molecules) to be accurately characterized by means of mass spectrometry through the determination of relative ion abundances. As a general trend, these measurements in the gas phase reveal that decorating naphthalene cations with a single sodium atom can increase the hydrogen attachment capacity by about 25% relative to the bare naphthalene cation, the effects being more significant when 3–7 hydrogen molecules are adsorbed. This enhancement reduces as we increase the number of H_2 around the PAH due to the shielding effect of the closer molecules on more external ones. Our computational modeling performed with two complementary approaches in which H_2 is treated as a rigid rotor or as a pseudo atom successfully reproduces this observation and shows that the enhanced adsorption is directly related to the preferential binding of H_2 to the alkali atom, over which a cap of 6–7 molecules can be formed until additional molecules necessarily bind, more weakly, to the aromatic hydrocarbon frame.

The present results provide the first experimental demonstration of the enhancement in hydrogen adsorption on polyaromatic substrates after decoration with a sodium cation, in the gas phase. Beyond this general trend, the experimental ion abundances also reveal particularly stable sizes for 2 and 7 hydrogen molecules in contact with bare and sodium-decorated protonated naphthalene, respectively, which were interpreted as magic numbers. While the prominent stability of the 2-molecule, undecorated cluster could be explained based on structural grounds alone, with hydrogen molecules sitting on both sides of the unprotonated aromatic cycle, the shell closure at size 7 could not be strictly reproduced, both models predicting instead a special stability at size 6 concomitant with the formation of a pentagonal ring of H_2 around the alkali with one extra capping molecule. The cause for this minor discrepancy could lie in the modeling itself, either in the unsufficiently accurate potential energy surfaces or in the excessively crude assumption that the cationic complex can be treated as rigid. It could also be due to some isomeric competition between low-lying forms of the hydrogen clusters separated by high energy barriers, making them virtually impossible to sample correctly by both the DMC and PIMD approaches. Such a situation is likely to occur if those isomers differ from the location of one or several H_2 molecules on either side of the aromatic.

We have also shown that the cationic PAHs are energetically favored by the addition of a Na atom, and that this trend is also maintained as more hydrogen molecules are adsorbed on the substrates. This effect is the strongest for the first 6–7 hydrogen molecules in the case of naphthalene. The PAHs present kinetic stability as determined from the HOMO-LUMO gap [71–73], with relatively minor effects upon the addition of a sodium atom. This stability is also supported by the analysis of the vibrational frequencies, as shown in Table S16 of the Supplementary Material. It is also worth noting that there are not significant differences between species that contain (protonated) or not an extra hydrogen atom, H, in stabilities or adsorption capabilities, they have been included in our analysis because they are more predominantly formed within the HNDs under the experimental conditions we use in this work.

Our modeling on larger hydrogen clusters and a broader diversity of PAHs indicates that the enhanced adsorption effect is local, hence the efficiency expected from larger polyaromatic compounds decorated with sodium remains uncertain. However, the situation could be different with other alkalis, for which the same computational methodology could be applied, and in particular potassium and of course lithium. Unfortunately, lithium would pose a greater challenge for gas phase experiments owing to the presence of isotopes. A recent computational investigation [74] suggested that once chemically adsorbed on graphene, lithium leads to higher hydrogen adsorption as compared to sodium at low coverage, although the situation reverts in favor of sodium once 4 hydrogen molecules are present. While large PAHs such as coronene are commonly considered as finite models of extended graphene, the aforecited paper confirms the interest in studying such molecules decorated with either alkali and the potential of fundamental approaches in the gas phase to untangle the effects of PAH size, structure, and the specific alkali atom on their propensity to reversibly bind hydrogen.

Although such cationic complexes in the gas phase are still far from being directly usable in hydrogen storage, they can still be considered as excellent prototype materials by themselves, or as a basis for other, more complex carbon-based materials, since they can be chemically synthesized rather easily [75] or combined in bottom-up approaches. In addition, it is the exposed surface of nanoporous materials that is their most important feature for hydrogen storage, and in particular, the binding energies they provide. In this respect, decorated carbon substrates provide relatively large binding energies compared with other materials [76], while remaining manageable and to a large extent tunable both from the experimental and theoretical points of view.

As far as computational models are concerned, they could also be extended to chemically more complex forms of carbon, such as nano- or mesoporous media possibly decorated with alkalis. Beyond structural and energetic considerations, another development worth considering could also lie in the kinetic aspects of the hydrogen adsorption–desorption process. In the present case, the scale of the interaction potentials and of the associated evaporation ranges between tens to almost 100 meV (up tp 10 kJ/mol), typical of non-covalent interactions,

and this leads to an efficient reversibility of the process. From appropriate time-dependent simulations or thermodynamical calculations [28], it would be useful to evaluate the characteristic pressure and temperature conditions of the reversible hydrogen storage. Such calculations should provide additional connections to the present gas phase experiments and, hopefully, shed light onto the subtle mechanisms explaining the magic numbers as well as the ability to adsorb and to desorb hydrogen from these substrates and the underlying mechanisms behind these processes. The possibilities for including more alkali atoms on the same PAH are also intriguing as well as their location on the substrate, as it is the competition between alkali versus aromaticity attraction in larger PAHs. We think that these are very interesting avenues that deserve to be investigated in the near future.

Declaration of competing interest

The authors declare that they have no known competing financial interests or personal relationships that could have appeared to influence the work reported in this paper.

Acknowledgments

This work was supported by the Austrian Science Fund, FWF (projects number W1259-N27 and P31149) and the Spanish MICINN with Grants PID2020-114654GB-I00/AEI/10.13039/501100011033, 2021–2024 (TGL,MB) and PID2020-114957GB-I00/AEI/10.13039/501100011033 (JCM, MIH). FC gratefully acknowledges support from the PSMN (Pôle Scientifique de Modélisation Numérique) of the ENS de Lyon for some of the computing resources.

Collaboration has also been supported by the CSIC under i-Link+ program LINKB20041. Allocation of computing time by CESGA (Spain) is also acknowledged.

Appendix A. Supplementary data

Supplementary material related to this article can be found online at https://doi.org/10.1016/j.ijhydene.2024.01.244.

References

[1] Abe J, Popoola A, Ajenifuja E, Popoola O. Hydrogen energy, economy and storage: Review and recommendation. Int J Hydrogen Energy 2019;44:15072–86.
[2] Capurso T, Stefanizzi M, Torresi M, Camporeale S. Perspective of the role of hydrogen in the 21st century energy transition. Energy Convers Manage 2022;251:114898.
[3] Faye O, Szpunar J, Eduok U. A critical review on the current technologies for the generation, storage, and transportation of hydrogen. Int J Hydrogen Energy 2022;47:13771–802.
[4] Ishaq H, Dincer I, Crawford C. A review on hydrogen production and utilization: Challenges and opportunities. Int J Hydrogen Energy 2022;47:26238–64.
[5] Langmi HW, Engelbrecht N, Modisha PM, Bessarabov D. Chapter 13 - Hydrogen storage. In: Smolinka T, Garche J, editors. Electrochemical power sources: Fundamentals, systems, and applications. Elsevier; 2022, p. 455–86.
[6] Bosu S, Rajamohan N. Recent advancements in hydrogen storage - comparative review on methods, operating conditions and challenges. Int J Hydrogen Energy 2024;52:352–70.
[7] Usman MR. Hydrogen storage methods: Review and current status. Renew Sustain Energy Rev 2022;167:112743.
[8] Huang Y, Cheng Y, Zhang J. A review of high density solid hydrogen storage materials by pyrolysis for promising mobile applications. Ind Eng Chem Res 2021;60:2737–71.
[9] Mohan M, Sharma VK, Kumar EA, Gayathri V. Hydrogen storage in carbon materials-A review. Energy Storage 2019;1:e35.
[10] Epelle EI, Desongu KS, Obande W, Adeleke AA, Ikubanni PP, Okolie JA, Gunes B. A comprehensive review of hydrogen production and storage: A focus on the role of nanomaterials. Int J Hydrogen Energy 2022;47:20398–431.
[11] Ren J, Musyoka NM, Langmi HW, Mathe M, Liao S. Current research trends and perspectives on materials-based hydrogen storage solutions: A critical review. Int J Hydrogen Energy 2017;42:289–311.
[12] Jain V, Kandasubramanian B. Functionalized graphene materials for hydrogen storage. J Mater Sci 2020;55:1865–903.
[13] Kojima Y. Hydrogen storage materials for hydrogen and energy carriers. Int J Hydrogen Energy 2019;44:18179–92.
[14] Hirscher M, Yartys VA, Baricco M, Bellosta von Colbe J, Blanchard D, Bowman RC, Broom DP, Buckley CE, Chang F, Chen P, Cho YW, Crivello J-C, Cuevas F, David WIF, de Jongh PE, Denys RV, Dornheim M, Felderhoff M, Filinchuk Y, Froudakis GE, Grant DM, Gray EM, Hauback BC, He T, Humphries TD, Jensen TR, Kim S, Kojima Y, Latroche M, Li H-W, Lototskyy MV, Makepeace JW, Møller KT, Naheed L, Ngene P, Noréus D, Nygård MM, Orimo S-I, Paskevicius M, Pasquini L, Ravnsbæk DB, Veronica Sofianos M, Udovic TJ, Vegge T, Walker GS, Webb CJ, Weidenthaler C, Zlotea C. Materials for hydrogen-based energy storage - past, recent progress and future outlook. J Alloys Compd 2020;827:153548.
[15] Zhang L, Allendorf MD, Balderas-Xicohténcatl R, Broom DP, Fanourgakis GS, Froudakis GE, Gennett T, Hurst KE, Ling S, Milanese C, Parilla PA, Pontiroli D, Riccò M, Shulda S, Stavila V, Steriotis TA, Webb CJ, Witman M, Hirscher M. Fundamentals of hydrogen storage in nanoporous materials. Prog Energy 2022;4:042013.
[16] Anikina E, Naqvi SR, Bae H, Lee H, Luo W, Ahuja R, Hussain T. High-capacity reversible hydrogen storage properties of metal-decorated nitrogenated holey graphenes. Int J Hydrogen Energy 2022;47:10654–64.
[17] Shet SP, Shanmuga Priya S, Sudhakar K, Tahir M. A review on current trends in potential use of metal–organic framework for hydrogen storage. Int J Hydrogen Energy 2021;46:11782–803.
[18] Kapelewski MT, Runčevski T, Tarver JD, Jiang HZH, Hurst KE, Parilla PA, Ayala A, Gennett T, FitzGerald SA, Brown CM, Long JR. Record high hydrogen storage capacity in the metal–organic framework Ni_2 (*m*-dobdc) at near-ambient temperatures. Chem Mater 2018;30:8179–89.
[19] Dündar-Tekkaya E, Yürüm Y. Mesoporous MCM-41 material for hydrogen storage: A short review. Int J Hydrogen Energy 2016;41:9789–95, special Issue: 1st International Symposium on Materials for Energy Storage and Conversion (mESC-IS 2015).
[20] Srinivasu K, Chandrakumar KRS, Ghosh SK. Computational investigation of hydrogen adsorption by alkali-metal-doped organic molecules: Role of aromaticity. ChemPhysChem 2009;10:427–35.
[21] Ghosh A, Debnath T, Ash T, Das AK. Multiple Li^+- and Mg^{2+}-decorated PAHs: potential systems for reversible hydrogen storage. RSC Adv 2017;7:9521–33.
[22] Tachikawa H, Iyama T. Mechanism of hydrogen storage in the graphene nanoflake-lithium-H_2 system. J Phys Chem C 2019;123:8709–16.
[23] Kalenchuk A, Bogdan V, Dunaev S, Kustov L. Influence of steric factors on reversible reactions of hydrogenation-dehydrogenation of polycyclic aromatic hydrocarbons on a Pt/C catalyst in hydrogen storage systems. Fuel 2020;280:118625.
[24] Storage H. 2023, https://www.energy.gov/eere/fuelcells/hydrogen-storage.
[25] Bartolomei M, Pérez de Tudela R, Arteaga K, González-Lezana T, Hernández MI, Campos-Martínez J, Villarreal P, Hernández-Rojas J, Bretón J, Pirani F. Adsorption of molecular hydrogen on coronene with a new potential energy surface. Phys Chem Chem Phys 2017;19:26358–68.
[26] Chandrakumar K, Ghosh SK. Alkali-metal-induced enhancement of hydrogen adsorption in C_{60} fullerene: An ab initio study. Nano Lett 2008;8:13–9.
[27] Teprovich JAJ, Wellons MS, Lascola R, Hwang S-J, Ward PA, Compton RN, Zidan R. Synthesis and characterization of a lithium-doped fullerane (Li_x-C_{60}-Hy) for reversible hydrogen storage. Nano Lett 2012;12:582–9.
[28] Sahoo RK, Chakraborty B, Sahu S. Reversible hydrogen storage on alkali metal (Li and Na) decorated C_{20} fullerene: A density functional study. Int J Hydrogen Energy 2021;46:40251–61.
[29] Ren J, Musyoka NM, Langmi HW, Mathe M, Liao S. Current research trends and perspectives on materials-based hydrogen storage solutions: A critical review. Int J Hydrogen Energy 2017;42:289–311.
[30] Yang RT. Hydrogen storage by alkali-doped carbon nanotubes–revisited. Carbon 2000;38:623–6.
[31] EL Kassaoui M, Lakhal M, Benyoussef A, El Kenz A, Loulidi M. Enhancement of hydrogen storage properties of metal–organic framework-5 by substitution (Zn, Cd and Mg) and decoration (Li, Be and Na). Int J Hydrogen Energy 2021;46:26426–36.
[32] Mauron P, Remhof A, Bliersbach A, Borgschulte A, Züttel A, Sheptyakov D, Gaboardi M, Choucair M, Pontiroli D, Aramini M, Gorreri A, Riccò M. Reversible hydrogen absorption in sodium intercalated fullerenes. Int J Hydrogen Energy 2012;37:14307–14.
[33] Zhou J, Wu MM, Zhou X, Sun Q. Tuning electronic and magnetic properties of graphene by surface modification. Appl Phys Lett 2009;95:103108.
[34] Murata Y, Calzolari A, Heun S. Tuning hydrogen adsorption on graphene by gate voltage. J Phys Chem C 2018;122:11591–7.
[35] Kaiser A, Renzler M, Kranabetter L, Schwärzler M, Parajuli R, Echt O, Scheier P. On enhanced hydrogen adsorption on alkali (cesium) doped C_{60} and effects of the quantum nature of the H_2 molecule on physisorption energies. Int J Hydrogen Energy 2017;42:3078–86.
[36] Laimer F, Kranabetter L, Tiefenthaler L, Albertini S, Zappa F, Ellis AM, Gatchell M, Scheier P. Highly charged droplets of superfluid helium. Phys Rev Lett 2019;123:165301.
[37] Tiefenthaler L, Ameixa J, Martini P, Albertini S, Ballauf L, Zankl M, Goulart M, Laimer F, von Haeften K, Zappa F, et al. An intense source for cold cluster ions of a specific composition. Rev Sci Instrum 2020;91:033315.

[38] Wang C, Tang C, Fu L. An effective method to screen carbon (boron, nitrogen) based two-dimensional hydrogen storage materials. Int J Hydrogen Energy 2020;45:25054–64.

[39] Gomez LF, Loginov E, Sliter R, Vilesov AF. Sizes of large He droplets. J Chem Phys 2011;135:154201.

[40] Albertini S, Gruber E, Zappa F, Krasnokutski S, Laimer F, Scheier P. Chemistry and physics of dopants embedded in helium droplets. Mass Spectrom Rev 2022;41:529–67.

[41] Atkins KR. Ions in liquid helium. Phys Rev 1959;116:1339–43.

[42] Mateo D, Gonzalez F, Eloranta J. Rotational superfluidity in small helium droplets. J Phys Chem A 2015;119:2262–70.

[43] Kollotzek S, Campos-Martínez J, Bartolomei M, Pirani F, Tiefenthaler L, Hernández MI, Lázaro T, Zunzunegui-Bru E, González-Lezana T, Bretón J, Hernández-Rojas J, Echt O, Scheier P. Helium nanodroplets as an efficient tool to investigate hydrogen attachment to alkali cations. Phys Chem Chem Phys 2023;25:462–70.

[44] Hunter EPL, Lias SG. Evaluated gas phase basicities and proton affinities of molecules: An update. J Phys Chem Ref Data 1998;27:413–656.

[45] Bartolomei M, Pirani F, Marques JMC. Aggregation enhancement of coronene molecules by seeding with alkali-metal. Phys Chem Chem Phys 2019;21:16005–16.

[46] Ortiz de Zárate J, Bartolomei M, González-Lezana T, Campos-Martínez J, Hernández MI, Pérez de Tudela R, Hernández-Rojas J, Bretón J, Pirani F, Kranabetter L, Martini P, Kuhn M, Laimer F, Scheier P. Snowball formation for Cs^+ solvation in molecular hydrogen and deuterium. Phys Chem Chem Phys 2019;21:15662–8.

[47] Kendall RA, Dunning TH, Harrison RJ. Electron affinities of the first-row atoms revisited. Systematic basis sets and wave functions. J Chem Phys 1992;96:6796–806.

[48] Pirani F, Brizi S, Roncaratti L, Casavecchia P, Cappelletti D, Vecchiocattivi F. Beyond the Lennard-Jones model: a simple and accurate potential function probed by high resolution scattering data useful for molecular dynamics simulations. Phys Chem Chem Phys 2008;10:5489–503.

[49] Halkier A, Helgaker T, Jorgensen P, Klopper W, Koch H, Olsen J, Wilson AK. Basis-set convergence in correlated calculations on Ne, N_2, and H_2O. Chem Phys Lett 1998;286:243–52.

[50] Halkier A, Helgaker T, Jorgensen P, Klopper W, Olsen J, Wilson AK. Basis-set convergence of the energy in molecular Hartree-Fock calculations. Chem Phys Lett 1999;302:437–46.

[51] Boys S, Bernardi F. The calculation of small molecular interactions by the differences of separate total energies. some procedures with reduced errors. Mol Phys 1970;19:553–66.

[52] Werner H-J, Knowles PJ, Lindh R, Manby FR, Schütz M, Celani P, Korona T, Rauhut G, Amos RD, Bernhardsson A, Berning A, Cooper DL, Deegan MJO, Dobbyn AJ, Eckert F, Hampel C, Hetzer G, Lloyd AW, McNicholas SJ, Meyer W, Mura ME, Nicklass A, Palmieri P, Pitzer R, Schumann U, Stoll H, Stone AJ, Tarroni R, Thorsteinsson T. Molpro, version2012.1, a package of ab initio programs. 2012, see http://www.molpro.net.

[53] Patkowski K, Cencek W, Jankowski P, Szalewicz K, Mehl JB, Garberoglio G, Harvey AH. Potential energy surface for interactions between two hydrogen molecules. J Chem Phys 2008;129:094304.

[54] Calvo F, Yurtsever E. Solvation of carbonaceous molecules by para-H_2 and ortho-D_2 clusters. I. Polycyclic aromatic hydrocarbons. J Chem Phys 2016;144:224302.

[55] Calvo F, Yurtsever E. Solvation of coronene oligomers by para-H_2 molecules: the effects of size and shape. Phys Chem Chem Phys 2020;22:12465–75.

[56] Silvera IF, Goldman VV. The isotropic intermolecular potential for H_2 and D_2 in the solid and gas phases. J Chem Phys 2008;69:4209–13.

[57] Wille L. Minimum-energy configurations of atomic clusters: new results obtained by simulated annealing. Chem Phys Lett 1987;133:405–10.

[58] Wales DJ, Doye JPK. Global optimization by basin-hopping and the lowest energy structures of Lennard-Jones clusters containing up to 110 atoms. J Phys Chem A 1997;101:5111–6.

[59] Anderson JB. A random–walk simulation of the Schrödinger equation: H_3^+. J Chem Phys 1975;63:1499–503.

[60] Suhm MA, Watts RO. Quantum monte carlo studies of vibrational states in molecules and clusters. Phys Rep 1991;204:293–329.

[61] Buch V. Treatment of rigid bodies by diffusion Monte-Carlo. Application to the para-H_2...H_2O and ortho-H_2...H_2O clusters. J Chem Phys 1992;97:726–9.

[62] Sandler P, Buch V, Sadlej J. Ground and excited states of the complex of CO with water: A diffusion Monte Carlo study. J Chem Phys 1996;105:10387–97.

[63] Sandler P, Buch V. General purpose QCLUSTER program for Rigid Body Diffusion Monte Carlo simulation of an arbitrary molecular cluster. 1999, (private communication).

[64] Pérez A, Tuckerman ME, Müser MHA. A comparative study of the centroid and ring-polymer molecular dynamics methods for approximating quantum time correlation functions from path integrals. J Chem Phys 2009;130:184105.

[65] Ralser S, Postler J, Harnisch M, Ellis AM, Scheier P. Extracting cluster distributions from mass spectra: Isotopefit. Int J Mass Spectrom 2015;379:194–9.

[66] Klots CE. The evaporative ensemble. Z Phys D 1987;5:83–9.

[67] Klots CE. Evaporation from small particles. J Phys Chem 1988;92:5864–8.

[68] Leidlmair C, Wang Y, Bartl P, Schöbel H, Denifl S, Probst M, Alcamí M, Martín F, Zettergren H, Hansen K, Echt O, Scheier P. Structures, energetics, and dynamics of helium adsorbed on isolated fullerene ions. Phys Rev Lett 2012;108:076101.

[69] An der Lan L, Bartl P, Leidlmair C, Jochum R, Denifl S, Echt O, Scheier P. Solvation of Na^+, K^+ and their dimers in helium. Chem Eur J 2012;18:4411.

[70] González-Lezana T, Echt O, Gatchell M, Bartolomei M, Campos-Martínez J, Scheier P. Solvation of ions in helium. Int Rev Phys Chem 2020;39:465–516.

[71] Ruiz-Morales Y. Homo-lumo gap as an index of molecular size and structure for polycyclic aromatic hydrocarbons (pahs) and asphaltenes: A theoretical study. i. J Phys Chem A 2002;106:11283–308.

[72] Ruiz-Morales Y. The agreement between clar structures and nucleus-independent chemical shift values in pericondensed benzenoid polycyclic aromatic hydrocarbons: An application of the y-rule. J Phys Chem A 2004;108:10873–96.

[73] Gutman I, Ruiz-Morales Y. Note on the y-rule in clar theory. Polycycl Aromat Compd 2007;27:41–9.

[74] Tachikawa H, Yi H, Iyama T, Yamasaki S, Azumi K. Hydrogen storage mechanism in sodium-based graphene nanoflakes: A density functional theory study. Hydrogen 2022;3:43–52.

[75] Tang M, Yu Q, Wang Z, Zhang C, Sun B, Yi Y, Zhang F-L. Synthesis of polycyclic aromatic hydrocarbons (PAHs) via a transient directing group. Org Lett 2018;20:7620–3.

[76] Allendorf MD, Hulvey Z, Gennett T, Ahmed A, Autrey T, Camp J, Seon Cho E, Furukawa H, Haranczyk M, Head-Gordon M, Jeong S, Karkamkar A, Liu D-J, Long JR, Meihaus KR, Nayyar IH, Nazarov R, Siegel DJ, Stavila V, Urban JJ, Veccham SP, Wood BC. An assessment of strategies for the development of solid-state adsorbents for vehicular hydrogen storage. Energy Environ Sci 2018;11:2784–812.